

A multi-model ensemble system for the Outer Heliosphere (MMESH): solar wind conditions near Jupiter

Article

Accepted Version

Rutala, M. J. ORCID: <https://orcid.org/0000-0002-1837-4057>,
Jackman, C. M. ORCID: <https://orcid.org/0000-0003-0635-7361>, Owens, M. J. ORCID: <https://orcid.org/0000-0003-2061-2453>, Tao, C. ORCID: <https://orcid.org/0000-0001-8817-0589>,
Fogg, A. R. ORCID: <https://orcid.org/0000-0002-1139-5920>,
Murray, S. A. ORCID: <https://orcid.org/0000-0002-9378-5315>
and Barnard, L. ORCID: <https://orcid.org/0000-0001-9876-4612> (2024) A multi-model ensemble system for the Outer
Heliosphere (MMESH): solar wind conditions near Jupiter.
Journal of Geophysical Research: Space Physics, 129 (6).
e2024JA032613. ISSN 2169-9402 doi: [10.1029/2024JA032613](https://doi.org/10.1029/2024JA032613)
Available at <https://centaur.reading.ac.uk/116874/>

It is advisable to refer to the publisher's version if you intend to cite from the work. See [Guidance on citing](#).

To link to this article DOI: <http://dx.doi.org/10.1029/2024JA032613>

Publisher: American Geophysical Union

All outputs in CentAUR are protected by Intellectual Property Rights law, including copyright law. Copyright and IPR is retained by the creators or other copyright holders. Terms and conditions for use of this material are defined in the [End User Agreement](#).

www.reading.ac.uk/centaur

CentAUR

Central Archive at the University of Reading

Reading's research outputs online

**A Multi-Model Ensemble System for the outer
Heliosphere (MMESH): Solar Wind Conditions near
Jupiter**

M. J. Rutala¹, C. M. Jackman¹, M. J. Owens², C. Tao³, A. R. Fogg¹, S. A. Murray¹

¹School of Cosmic Physics, DIAS Dunsink Observatory, Dublin Institute for Advanced Studies, Dublin, Ireland

²Department of Meteorology, University of Reading, Earley Gate, PO Box 243, Reading RG6 6BB, UK

³Space Environment Laboratory, National Institute of Information and Communications Technology (NICT), Koganei, Japan

Key Points:

- The performance of several existing solar wind propagation models at the orbit of Jupiter is measured for multiple spacecraft epochs.
- A flexible system is developed to generate an ensemble of multiple propagation models in order to best leverage each input model's strengths.
- Over the epoch tested, the multi-model ensemble outperforms individual input models by 7% – 110% in forecasting the solar wind flow speed.

18 **Abstract**

19 How the solar wind influences the magnetospheres of the outer planets is a fundamen-
 20 tally important question, but is difficult to answer due to the lack of consistent upstream
 21 monitoring of the interplanetary medium (IPM) and the large-scale dynamics internal
 22 to the magnetosphere. This makes it very challenging to link external drivers with the
 23 magnetospheric dynamics measured by a single orbiting spacecraft. To compensate for
 24 the relative lack of in-situ data, solar wind propagation models are often used to esti-
 25 mate the ambient IPM conditions at the outer planets for comparison to remote obser-
 26 vations or in-situ measurements. This introduces another complication: the propaga-
 27 tion of near-Earth measurements of the solar wind introduces uncertainties in both tim-
 28 ing and magnitude which are themselves difficult to assess. Here, we present the Multi-
 29 Model Ensemble System for the outer Heliosphere (MMESH) to begin to address these
 30 issues, along with the resultant multi-model ensemble (MME) of the solar wind condi-
 31 tions near Jupiter as a means to assess the system. MMESH accepts as input any num-
 32 ber of solar wind models together with contemporaneous in-situ spacecraft data. From
 33 these, the system characterizes typical uncertainties in model timing, quantifies how these
 34 uncertainties vary under different conditions and time periods, attempts to correct for
 35 systematic biases in the input model timing, and composes a multi-model ensemble (MME)
 36 with uncertainties from the results. For the case of the Jupiter-MME here, three solar
 37 wind propagation models were compared to in-situ measurements from near-Jupiter space-
 38 craft spanning diverse spacecraft-Sun-Earth alignments and phases of the solar cycle, amount-
 39 ing to more than 23,000 hours over four decades. The resulting MME produces the most-
 40 probable near-Jupiter IPM conditions for times within the tested epoch. Finally, we will
 41 discuss how the work presented here can be extended towards more robust character-
 42 ization of solar wind parameters and time-dependent propagation of solar wind condi-
 43 tions at other planetary magnetospheres.

44 **1 Background**

45 The solar wind is a continuous stream of plasma emanating from the Sun in all di-
 46 **rections which** evolves as it travels through the heliosphere, interacting with every plan-
 47 etary magnetosphere in the solar system along the way. Near the Earth, the typical val-
 48 ues of the solar wind flow speed $u_{mag,\oplus}$ (324–584 km/s), proton density n_{\oplus} (2.2–12.7 cm⁻³),
 49 dynamic (ram) pressure $p_{dyn,\oplus}$ (0.86–3.92 nPa), and interplanetary magnetic field (IMF)
 50 magnitude $B_{mag,\oplus}$ (3.1–9.7) nT have all been statistically characterized by the expan-
 51 sive OMNI dataset (King & Papitashvili, 2005; Papitashvili & King, 2020), with values
 52 here spanning the start of OMNI2 to the start of 2023 (1963/11/27 – 2023/01/01) and
 53 characterizing 80% (10th – 90th percentiles) of all measurements. The OMNI dataset
 54 is a composite of many near-Earth observations encompassing some 19 total spacecraft
 55 over its full time domain, including most recently *Wind* (Lepping et al., 1995; Kasper,
 56 2002; King & Papitashvili, 2005) and ACE (D. J. McComas et al., 1998; Smith et al.,
 57 1998; King & Papitashvili, 2005).

58 While fewer in-situ heliospheric data are available in the outer solar system, the
 59 average solar wind conditions have still been constrained by the various spacecraft to visit
 60 the outer planets, whether during planetary flyby or approach. At Jupiter, the most-visited
 61 of the outer planets, the solar wind has been characterized during the flybys of *Pioneers*
 62 *10* and *11*, *Voyagers 1* and *2*, *Ulysses*, *Cassini*, and *New Horizons* (e.g. Slavin et al., 1985;
 63 J. D. Richardson et al., 1995; Ebert et al., 2014; Hanlon et al., 2004; Ebert et al., 2010).
 64 Compared to flybys, orbiter missions, including *Galileo* and *Juno* at Jupiter, generally
 65 provide fewer in-situ data: these missions have close-in orbits to best study the planet
 66 itself, thus setting them deep inside the planet's magnetosphere and shielding them from
 67 the solar wind. As a result, they only sample the wind during the planetary approach
 68 phase prior to orbital insertion and occasional excursions into the solar wind near apo-
 69 apsis. The polar solar orbiter *Ulysses* gives the best single-spacecraft characterization of

70 the average near-Jupiter solar wind owing to its 18-year lifetime: 80% of *Ulysses* measurements span 380–520 km/s in solar wind flow speed u_{mag} , 0.05–0.55 cm $^{-3}$ in plasma density n , 0.02–0.20 nPa in dynamic pressure p_{dyn} , and 0.22–1.5 nT in IMF magnitude B_{IMF} (Ebert et al., 2014). Despite a large number of measurements, these reported distributions are only approximate due to the polar orbit of the *Ulysses* spacecraft; *Ulysses* samples the solar wind in the ecliptic plane periodically, and these numbers were drawn from two non-consecutive spans at different phases of the solar cycle— one with a slower, cooler, and denser average solar wind than the other (Ebert et al., 2014).

78 The highly dynamic nature of the solar wind is not captured by these average values.
 79 Singular events, such as the eruption of coronal mass ejections (CMEs), and their
 80 propagation through the heliosphere as interplanetary coronal mass ejections (ICMEs),
 81 are a major source of short timescale variation in the measured solar wind (Palmerio et
 82 al., 2021, and references therein). In terms of the quantities already discussed, interplan-
 83 etary coronal mass ejections (ICMEs) show expansion, which manifests in measurements
 84 as an increase in u_{mag} at the leading edge and a decrease at the trailing edge, large drops
 85 in n , and an enhancement in B_{IMF} magnitude but decrease in B_{IMF} variance (Zurbuchen
 86 & Richardson, 2006; M. J. Owens, 2018). Beyond these events, the ambient solar wind
 87 is dynamic due to the presence of two different streaming plasma populations originat-
 88 ing in different regions of the solar corona: a comparatively fast, hot, and tenuous stream
 89 and a comparatively slow, cool, and dense stream (Crooker et al., 1999). These streams
 90 are essentially bimodal during solar minimum, with fast streams originating at high he-
 91 liolatitude and slow streams originating nearer the solar equator (D. J. McComas et al.,
 92 1998, 2000); during solar maximum, these streams are markedly less ordered (D. J. Mc-
 93 Comas et al., 2003). From solar cycle to solar cycle, the bulk parameters of the fast stream
 94 in particular can change dramatically (D. McComas et al., 2008; Ebert et al., 2009; D. J. Mc-
 95 Comas et al., 2013; Ebert et al., 2014). As different regions of the sun rotate underneath,
 96 corotating interacting regions (CIRs) are formed where a fast flow catches up to a slow
 97 flow; this process is common throughout the heliosphere (I. G. Richardson, 2018) and
 98 drives significant interactions with planetary magnetospheres, including at the Earth (Crooker
 99 et al., 1999; Gosling & Pizzo, 1999; Tsurutani et al., 2006; Borovsky & Denton, 2010)
 100 and at Jupiter (D. J. McComas et al., 2003; Hanlon et al., 2004; Ebert et al., 2014).

101 In-situ-data-driven statistical studies of the time variable solar wind at specific lo-
 102 cations within the outer heliosphere (e.g. at Jupiter) are hampered by the limited tem-
 103 poral coverage of visiting spacecraft; there is no continuous composite model like OMNI
 104 for any outer planet. Such statistical studies often instead have solar wind data supple-
 105 mented by solar wind propagation models, which attempt to reproduce the time-varying
 106 solar wind at one location from measurements at another location at which the solar wind
 107 is known. Many of these models have been employed in the outer heliosphere, includ-
 108 ing, but not limited to, the model of Tao et al. (2005) (“Tao+”, hereafter), ENLIL (Odstrcil,
 109 2003), mSWiM (Zieger & Hansen, 2008), HUXt (Barnard & Owens, 2022; M. Owens et
 110 al., 2020), and MSWIM2D (Keebler et al., 2022). These models all differ in their dimen-
 111 sionality, the simplifications made to the magnetohydrodynamics (MHD) equations un-
 112 derlying them, and the source of the input solar wind conditions used to initialize the
 113 model. By virtue of modelling solar wind conditions for times and locations where no
 114 in-situ spacecraft measurements are available, the outputs of these models cannot be di-
 115 rectly compared to data in typical usage scenarios. Generally, solar wind propagation
 116 models are instead compared to in-situ spacecraft measurements at times and locations
 117 where they are available in order to approximate the model errors— generally, shock ar-
 118 rival time (or “timing”) errors— prior to being used to supplement the data (Tao et al.,
 119 2005; Zieger & Hansen, 2008; Keebler et al., 2022). Measured timing uncertainties can
 120 be as high as ± 4 days and often trends with other physical parameters of the system,
 121 such as with Target-Sun-Observer (TSO) angle (Tao et al., 2005; Zieger & Hansen, 2008;
 122 Keebler et al., 2022) or with phase of the solar cycle (Zieger & Hansen, 2008).

123 These resulting time-varying timing uncertainties introduce a challenge in interpreting the results of these models and performing statistical analyses, particularly because the characterizations of timing uncertainty in each propagation model are often
 124 not measured by the same methods, and thus are not directly comparable to one another.
 125 Timing uncertainties can be measured by manually identifying shocks and shock-like structures in both modeled and measured solar wind time series and comparing their occurrence times (e.g. Tao et al., 2005) or by offsetting one time series relative to the other and maximizing the resulting prediction efficiency, or Pearson correlation coefficient (e.g.
 126 Zieger & Hansen, 2008). Measuring uncertainties with the latter method implies that
 127 a single timing uncertainty characterizes the model over the full time period inspected.
 128 An alternative to this is to employ dynamic time warping to explicitly allow for time-
 129 varying timing uncertainties (e.g. Samara et al., 2022). If these model uncertainties
 130 were quantified in a cross-model-consistent manner, the time-varying uncertainties could
 131 be accounted for and partially mitigated. For instance, as propagation model output un-
 132 certainties are known to trend with physical quantities, each individual model's outputs
 133 could be de-trended with sufficient characterization of the uncertainties. Alternatively,
 134 a multi-model ensemble (MME) could be composed by cross-comparison of the models
 135 in order to mitigate uncertainties. An MME is, in essence, a weighted average of differ-
 136 ent model outputs (Murray, 2018); the weighting scheme can be adjusted based on met-
 137 rics of the models performance (or “skill”) during intervals where in-situ data are avail-
 138 able (Murray, 2018; Elvidge et al., 2023). Ideally, fully-independent models would be used
 139 in an MME, so that they would be expected to have independent random errors which
 140 would thus tend to cancel, rather than add (Hagedorn et al., 2005; Riley et al., 2018).
 141 If all input models capture the same physics, outperform one another in different param-
 142 eter spaces, and have independent errors, a MME of these models should describe the
 143 underlying physical system more accurately than any individual input.
 144

145 Here we present the Multi-Model Ensemble System for the outer Heliosphere (MMESH):
 146 a framework to quantify and mitigate timing uncertainties in solar wind propagation mod-
 147 els and produce a single prediction by combining all of these approaches. This system
 148 allows for the automatic quantification of model timing uncertainties, trending of tim-
 149 ing uncertainties with physically relevant parameters, de-trending of the original model
 150 timing, and combination of distinct models into a single MME. MMESH is designed to
 151 flexibly compare any combination of input solar wind propagation models and contem-
 152 poraneous in-situ data in order to create an MME. To demonstrate this concretely, here
 153 we construct an MME of the solar wind conditions at Jupiter during the *Juno* era.
 154

155 Thus prior to discussing MMESH itself, we first discuss the in-situ spacecraft datasets
 156 to be used for comparison (Section 2.1) and give some introduction to the specific so-
 157 lar wind propagation models considered here (Section 2.2). We then introduce the MMESH
 158 framework in Section 3, beginning with a description of the statistical techniques and
 159 tools used to compare models, including the MME, to contemporaneous data and mea-
 160 sure their performance (Section 3.1). In Section 3.2 we discuss the methods available to
 161 characterize the model timing uncertainties relative to the in-situ time series: constant
 162 time offsetting (Section 3.2.1) and dynamic time warping (DTW, Section 3.2.2). We then
 163 proceed to describe how trends in the empirical timing uncertainties are characterized
 164 and estimated for epochs without contemporaneous in-situ data (Section 3.3) before dis-
 165 cussing the composition (Section 3.4) and performance (Section 3.4.1) of the multi-epoch
 166 MME composed of the de-trended models. Having described MMESH, we then present
 167 the MME of the solar wind conditions at Jupiter for the first 7 years of the *Juno* mis-
 168 sion, spanning 2016/7/4 – 2023/7/4, for use in future statistical analyses (Section 4),
 169 prior to concluding.
 170

Table 1. In-situ measurements of solar wind parameters near Jupiter’s orbit.

Mission	Coverage [yyyy/mm/dd]	Range [AU]	Heliolatitude [deg]	Measurements [hr]
<i>Ulysses</i>	1991/12/08 – 1992/02/02	4.90 – 5.41	–6.10 – +6.10	1,344
	1997/08/14 – 1998/04/16	4.90 – 5.41	–6.10 – +6.10	5,878
	2003/10/24 – 2004/06/22	4.90 – 5.41	–6.10 – +6.10	5,801
<i>Juno</i>	2016/05/15 – 2016/06/29	5.27 – 5.44	–5.76 – –5.23	1,080

173 2 Inputs

174 2.1 Solar Wind Data

175 The present aim for the MME framework discussed here is to find the most accurate
 176 combination of solar wind models in the near-Jupiter region of the outer heliosphere.
 177 As such, limiting the data included for comparison to the input and ensemble models
 178 to that which is representative of conditions at Jupiter is essential. Including too large
 179 a range of radial or helio-latitudinal in-situ measurements risks including different regimes
 180 of solar wind properties which the models are not, and should not be, expected to re-
 181 produce. This is particularly an issue in choosing a useful range of heliolatitude— too nar-
 182 row a range and the amount of data available shrinks, but too large a range and the faster
 183 solar wind flows at higher heliolatitudes are included erroneously. This issue primarily
 184 relates to data acquired by the *Ulysses* spacecraft, which is a solar polar orbiter. Pre-
 185 vious *Ulysses* measurements show that, during solar minimum when the latitudinal struc-
 186 ture of the solar wind is well-ordered, the equatorial slow solar wind zone may extend
 187 to $\pm 20^\circ$ – $\pm 30^\circ$ about the solar equator (D. J. McComas et al., 2003). Ebert et al. (2014)
 188 further restricts this range in surveying near-Jupiter solar wind conditions measured with
 189 *Ulysses* and selects for data $\pm 10^\circ$ about the solar equator 

190 Here, the near-Jupiter outer heliosphere is defined as the region of the heliosphere
 191 spanning $4.9 \text{ AU} < r < 5.5 \text{ AU}$ for spherical distance from the Sun r and $-6.1^\circ \leq$
 192 $\theta \leq 6.1^\circ$ for heliolatitude θ . Jupiter’s perihelion and aphelion (5.04 and 5.37 AU, re-
 193 spectively) fit entirely within this range, which includes padding of $\sim 0.15 \text{ AU}$, or ap-
 194 proximately 50%, on either end to increase the number of observations included. The
 195 heliolatitude range selected represents the maximal range of Jupiter’s location in heli-
 196 olatitude without any padding in order to avoid unrealistic sampling of the high latitude
 197 fast solar wind flows.

198 Several spacecraft have transited this region, including *Pioneers 10* and *11*, *Voy-*
 199 *agers 1* and *2*, *Ulysses*, *Galileo*, *Cassini*, *New Horizons* and *Juno*. Here, just data from
 200 just the *Ulysses* and *Juno* missions are used; the remaining spacecraft are not used in
 201 this analysis either due to being discontinuous at temporal resolutions of 1 hour (*Galileo*, *Cassini*,
 202 and *New Horizons*) or due to a lack of coverage in all or some of the models to be dis-
 203 cussed in Section 2.2 (*Pioneers 10* and *11* and *Voyagers 1* and *2*). A brief overview of
 204 the used spacecraft trajectories and data is included in Table 1 and the durations of the
 205 visits of these spacecraft to the near-Jupiter outer heliosphere is illustrated in Figure 1
 206 relative to the solar cycle, as measured by F10.7 radio flux derived from observations at
 207 the Dominion Radio Astrophysical Observatory (DRAO) and adjusted to account for
 208 variations in the Earth’s distance from the Sun. While the majority of these spacecraft
 209 passed near Jupiter, the *Ulysses* spacecraft, as a polar orbiter, transits through the near-
 210 Jovian outer heliosphere away from the planet itself after its initial Jupiter flyby. The
 211 relevant orbital components for all the spacecraft in Table 1 are shown in Figure 2, which
 212 highlights the rarity of near-Jupiter outer heliosphere measurements made far from Jupiter
 213 itself and the comparative evenness of coverage in Target-Sun-Earth angle.

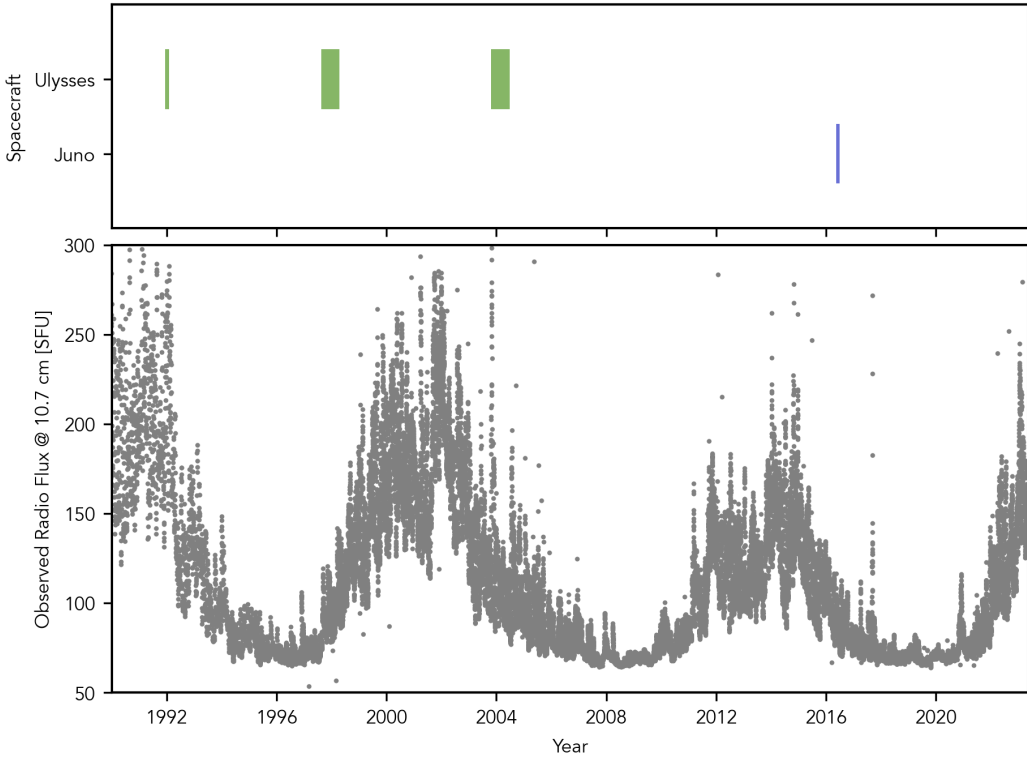


Figure 1. The (a) spans during which each spacecraft used in this analysis was measuring the near-Jupiter solar wind compared with the (b) solar F10.7 cm radio flux, a proxy for the phase of the solar cycle, over the period 1990-2023. Spacecraft coverage spans the ascending and descending phases of the solar cycle, but largely excludes solar minimum and solar maximum. These spacecraft have been selected for the frequency of their plasma and magnetic field measurements, which are generally hourly or better.

All of the spacecraft referenced in Table 1 have both magnetometers and plasma instruments, and thus provide sampling of the interplanetary magnetic field (IMF) B_{IMF} , the solar wind ion number density n , and the magnitude of the solar wind flow speed u_{mag} , which is itself dominated by the radial component of the outward flow of the solar wind. As the proton density n_p is measured in all cases and protons are the dominant ion component of the solar wind (Ebert et al., 2014, e.g.), the total density of the solar wind is approximately equal to the proton density ($n \approx n_p$) and is assumed to be exactly equal in calculating the solar wind dynamic pressure $p_{dyn} = m_p n u_{mag}^2$, where m_p is the proton mass. Detailed descriptions of these instruments, including their heritages, limitations, and data products, are discussed in their respective instrument papers (Balogh et al., 1992; Bame et al., 1992; Connerney et al., 2017; D. J. McComas et al., 2017). Pre-processed data was obtained from the Goddard Space Flight Center (GSFC) Space Physics Data Facility (SPDF) COHOWeb archives, with the exception of *Juno* plasma data which was instead obtained from Wilson et al. (2018).

2.2 Solar Wind Models

While several solar wind propagation models for the outer heliosphere are available, three were chosen for detailed study and inclusion in the MME: the Tao+ (Tao et al., 2005), ENLIL (Odstrcil, 2003), and HUXt (M. Owens et al., 2020; Barnard & Owens,

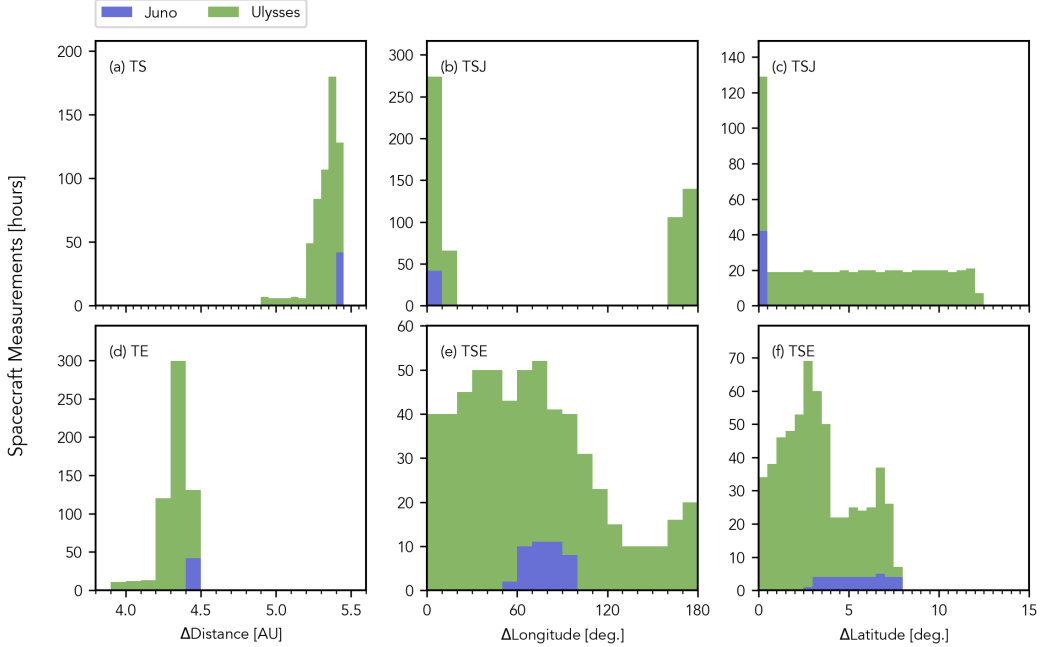


Figure 2. Histograms showing the spatial coverage of all the spacecraft used here, including the (a) Target-Sun (TS) distance, (b) Target-Sun-Jupiter (TSJ) longitude angle, (c) TSJ latitude angle, (d) Target-Earth (TE) distance, (e) Target-Sun-Earth (TSE) longitude angle, and (f) TSE latitude angle. The angles are measured in the Sun’s inertial reference frame, such that longitude measures distance along the solar equator and latitude measures perpendicular distances along the sphere of the Sun. The majority of spacecraft measurements occur very near Jupiter, with minimal separation in TSJ longitude or latitude angles. The unique coverage of the polar-orbiting *Ulysses* spacecraft stands out, and provides even coverage across TSJ, and to a lesser extent TSE, latitudes. Taking all spacecraft into consideration, the spatial coverage relative to the Earth’s location is fairly even.

232 models. These models in particular are ideal for inclusion in a MME due to their
 233 differing input parameters, dimensionality, and approaches to propagating the solar wind
 234 beyond the Earth, as is summarized in Table 2 and will be discussed further here.

Fundamentally, most models propagate solar wind conditions outwards by solving the system of equations which constitute MHD, these being: the continuity equation, the momentum equation, the equation of state, and several physical laws necessary to close the system (Faraday’s, Ohm’s, and Ampère’s laws). Propagation models differ primarily in their treatment of the momentum equation. For a single-species plasma composed of protons, this is:

$$\frac{\partial(m_p n \vec{u})}{\partial t} + \rho(\vec{u} \cdot \nabla) \vec{u} = - \underbrace{\nabla p}_{\text{pressure}} + \underbrace{\vec{j} \times \vec{B}}_{\text{Lorentz}} - \underbrace{\frac{GM_{\odot} \rho}{r^2} \hat{r}}_{\text{gravity}} + \underbrace{\nu \nabla^2 \vec{u}}_{\text{collision}} \quad (1)$$

235 where m_p is the proton mass, n is the plasma number density, \vec{u} is the plasma flow ve-
 236 locity, p is the total plasma pressure, \vec{j} is the plasma current density, \vec{B} is the ambient
 237 magnetic field, G is the gravitational constant, M_{\odot} is a solar mass, r is the radial dis-
 238 tance in a heliocentric spherical frame with the \hat{r} direction pointing radially outward,
 239 and ν is a collisional frequency. In Equation 1, the right-hand-side terms are labelled cor-

Table 2. Descriptive parameters of solar wind propagation models as used in this study.

Model	Type	Inner Boundary ^a [AU]	MHD Terms ^b (P, L, G, C)	Input ^a type (source)	Output ^c (n , u_{mag} , p_{dyn} , B_{IMF})
ENLIL	3D MHD	~0.1	(P, L, G)	remote (WSA)	(n , u_{mag} , p_{dyn} , B_{IMF})
HUXt	1D HD	~1	—	in-situ (OMNI)	(u_{mag})
Tao+	1D MHD	~1	(P, L, G)	in-situ (OMNI)	(n , u_{mag} , p_{dyn} , B_{IMF})

^a Inner boundaries and input types are reported for the versions of the models used here. The models are not necessarily limited to these inner boundaries and input types only, as described in the text.

^b The (P)ressure, (L)orentz, (G)ravitational, and (C)ollisional terms of the governing MHD momentum equation (Eqn. 1).

^c Components of the solar wind: plasma density (n), plasma flow speed (u_{mag}), plasma dynamic pressure (p_{dyn}), or IMF (B_{IMF}).

240 responding to the physical forces they represent, these being the (gradient) pressure, Lorentz,
 241 gravitational, and collisional forces, respectively. As summarized in Table 2, solar wind
 242 propagation models differ in which terms of the momentum equation they assume are
 243 insignificant in the solar wind. Most propagation models, including all those discussed
 244 here, do not consider collisional forces within the solar wind plasma. Both ENLIL and
 245 Tao+ keep all the remaining terms shown in Equation 1 (Tao et al., 2005; Odstrcil, 2003).
 246 HUXt assumes that all forces are negligible compared to the magnitude of the left-hand-
 247 side momentum terms in Equation 1, and thus does not consider any force terms (M. Owens
 248 et al., 2020).

249 The variables propagated by each model are directly related to the force terms that
 250 they consider in Equation 1, and are listed in Table 2 for the three models discussed here.
 251 The dimensionality of each model changes which components of the vector terms in Equa-
 252 tion 1 can be propagated; for cross-model consistency, we therefore compare solar wind
 253 parameter magnitudes rather than vector components, where each magnitude is calcu-
 254 lated as the root-sum-square of available components. The solar wind flow speed u_{mag}
 255 is thus available from all three propagation models considered here. **This is the only pa-**
 256 **rameter available from HUXt;** none of the solar wind density n , temperature T , or IMF
 257 strength B_{IMF} are propagated as these variables are eliminated from the version of the
 258 momentum equation used. These parameters— density n , temperature T , and IMF strength
 259 B_{IMF} of the propagated solar wind— are available from both ENLIL and Tao+.

260 Each of these models has an inner boundary at which the conditions of the solar
 261 wind are input and continuously updated over the course of the model run. The loca-
 262 tion of this inner boundary and the sources from which the input solar wind conditions
 263 are drawn vary between models and are summarized in Table 2. ENLIL takes as input
 264 a 3-dimensional description of the solar corona and near-sun environment, here supplied
 265 by the Wang-Sheeley-Arge (WAS) model (Arge & Pizzo, 2000) which itself takes remote
 266 observations of the sun as input. For this study, solar magnetograms from the Kitt Peak
 267 Observatory are used, with gaps in observations filled in by those from the Mount Wil-
 268 son Observatory. This sort of boundary is unique amongst the models considered here:
 269 HUXt and Tao+ instead take in-situ spacecraft measurements, or proxies thereof, as in-
 270 puts. In this study, both models take OMNI measurements at ~1 AU as inputs, although
 271 they both have the functionality to be run at any other location in the solar system, pro-
 272 vided there are sufficient in-situ solar wind data available (e.g. Sanchez-Diaz et al., 2016;
 273 Barnard & Owens, 2022). Accuracy in these input solar wind conditions are the single

274 largest factor in determining the propagated solar wind accuracy (Riley et al., 2018), and
 275 as such including a variety of inputs is beneficial to the final MME.

276 The input solar wind conditions used here are assumed to be sampled from the back-
 277 ground solar wind. This means that coronal mass ejections (CMEs) sampled at the model
 278 inner boundary are not propagated using the standard cone model (Zhao et al., 2002;
 279 Xie et al., 2004) but are instead interpreted as fast solar wind flows; rather than prop-
 280 agate CMEs as radially-expanding regions of constant angular size, they are treated by
 281 the same fluid description used by each model to describe the rest of the solar wind flow.
 282 This introduces an intrinsic error into the background solar wind parameters in all of
 283 the models. Future studies could mitigate this additional source of error by subtracting
 284 CMEs from the input data prior to propagation, then simultaneously propagating the
 285 quiescent solar wind and the CME using the cone model, but such an involved change
 286 to the modeling is ultimately beyond the current scope of this project.

287 These three models each run at different spatial and temporal resolutions which
 288 are directly related to their dimensionality and domains within the heliosphere, and which
 289 directly impact the small-scale shape of their output propagated solar wind estimates.
 290 ENLIL covers three spatial dimensions, spanning 0.1–10 AU radially at 0.02 AU res-
 291 olution, 360° in longitude at 2° resolution, and $\pm 60^\circ$ in latitude at 2° resolution, with
 292 a temporal resolution of 1 hour. HUXt is physically a one-dimensional radial model, but
 293 in practice here it is run in its two-dimensional form in order to more easily sample the
 294 model at the spacecraft position. Functionally, the two-dimensional form of HUXt is a
 295 series of independent one-dimensional models spanning 1–6 AU radially with a reso-
 296 lution of 0.007 AU, 360° in longitude at $\sim 2.8^\circ$ resolution, and an intrinsic temporal res-
 297 olution of 17.4 minutes in the version of the model used here. Tao+ spatial dimension,
 298 ranging from 1–8 AU at a resolution of 1/300 AU, with an intrinsic temporal resolu-
 299 tion of 10 s. The outputs of both HUXt and Tao+ have been downsampled to a reso-
 300 lution of 1 hour to better match the spacecraft data and other models for use in this study.

301 Figure 3 shows the model-propagated solar wind flow speed u_{mag} during the *Juno*
 302 cruise towards Jupiter compared with contemporaneous JADE in-situ measurements from
 303 Wilson et al. (2018) for each of the models detailed here. While these models are all able
 304 to propagate solar wind conditions during the other spacecraft epochs shown in Table
 305 1, and both ENLIL and Tao+ are able to propagate parameters other than u_{mag} , here
 306 we have chosen to show just a single-spacecraft and single-parameter comparison for il-
 307 lustrative purposes. The agreement between each model and the data in general form
 308 is clear, but significant deviations in the arrival time of large-scale shocks and smaller-
 309 scale increases in flow speed between the models and data are evident. These temporal
 310 lags, which represent single measurements of the full distribution of model timing un-
 311 certainties, appear to be of the same sign for Tao+ and HUXt but are substantially dif-
 312 ferent for ENLIL. Characterizing these differences in arrival time is critically important
 313 to understanding the accuracy of these models in propagating the solar wind, and will
 314 be further explored here.

315 3 Description of MMESH

316 The clear disagreements between the propagation models and in-situ data in both
 317 the modeled arrival time and magnitude, as illustrated in Figure 3, makes the need for
 318 careful consideration of uncertainties and new statistical approaches in solar wind prop-
 319 agation modeling evident. MMESH has been designed as a framework to tackle these
 320 issues. After briefly introducing the statistical metrics used in quantifying model per-
 321 formance (Section 3.1), the MMESH framework will be described. This system allows
 322 any number of solar wind propagation models to be compared to simultaneous in-situ
 323 data; from this comparison, timing uncertainties are characterized either as a constant
 324 value over the full duration of each model (i.e. as a bias, as explored in Section 3.2.1)

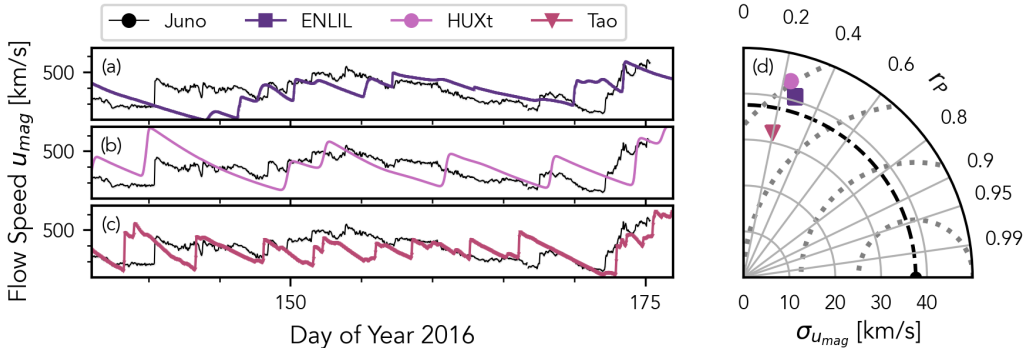


Figure 3. Measured solar wind flow speed u_{mag} from *Juno* JADE moments (Wilson et al., 2018) with the same from the (a) ENLIL, (b) HUXt, and (c) Tao+ models, as labeled, with (d) a Taylor diagram illustrating the performance of each model relative to the data, as discussed in Section 3.1. The flow speed is referenced as the root-mean-square of all velocity components, where components are available. Temporal lags in the timing of the modeled solar wind flow speed u_{mag} are apparent in all models, and are made evident by the Taylor diagram.

325 or as a dynamic value (Section 3.2.2). This framework fundamentally supports a multi-
 326 epoch analysis, in which the same timing uncertainties are quantified over multiple space-
 327 craft epochs, each with one set of in-situ data and multiple models, in order to better
 328 characterize the model timing uncertainties, including any timing biases (Section 3.3).
 329 From this characterization, the solar wind propagation models can then have any iden-
 330 tified biases in timing removed before being assembled into an MME (Section 3.4).

331 3.1 Performance Metrics

332 The correlation coefficient r , as a robust measure of model goodness-of-fit, is a good
 333 metric to be maximized in optimizing the alignment of solar wind model to data, as will
 334 be discussed in Section 3.2.1. For simple methods of aligning the model and data, the
 335 correlation coefficient r is sufficient alone as a metric. More complex methods of align-
 336 ment, such as discussed in Section 3.2.2, are better optimized while considering some penalty
 337 against increasing complexity, in order to maintain physical realism and interpretabil-
 338 ity. In this case, a statistic determined by both the correlation coefficient and some mea-
 339 sure of the width of the distribution of timing uncertainties is preferred for optimization.
 340 Such a statistic is less likely to reach its maximum value when a large range of timin-
 341 ing uncertainties are predicted, thus preventing unphysical alignment of a model with,
 342 for instance, a shock-like structure from a previous Carrington rotation. Within MMESH,
 343 we define σ_T to be the half-width containing 34% of the distribution of timing offsets,
 344 such that it would reduce to one standard deviation in a normal distribution. The op-
 345 timization metric for these cases is then defined as $r + (1 - \sigma_T/\Delta T)$, where ΔT repre-
 346 sents half the largest allowed magnitude of a timing uncertainty, such that the statis-
 347 tic varies between 0–2, with the former corresponding to the worst performance and
 348 the latter corresponding to the best.

349 Neither the correlation coefficient r nor the statistic r/σ_T as single numbers fully
 350 characterize how closely a model matches data on different scales. Combining the cor-
 351 relation coefficient r with the overall standard deviation of both the time series and the
 352 model residuals forms the basis for a more complete multi-scale comparison of model and
 353 data summarized by the Taylor diagram (Taylor, 2001), illustrated in Figure 6. This type
 354 of plot relates the standard deviation of the modeled time series, the correlation coef-
 355 ficient of the modeled time series relative to the measured time series, and the centered

356 root-mean-square difference between the modeled and measured time series to one another by analogy with the law of cosines, allowing all three quantities to be displayed
 357 as a single point on the diagram. This is particularly useful for comparing the performance
 358 of different models to one another on the same axes. All-around better models—
 359 those with high correlation coefficients, small residuals when compared with the data,
 360 and similar intrinsic variances— appear graphically closer to the point representing the
 361 data time series along the x-axis.

363 3.2 Characterization of Propagation Model Performance

364 The arrival time of shocks is of particular interest in statistical studies both at Jupiter
 365 and elsewhere in the outer heliosphere; the arrival of a shock is expected to compress the
 366 magnetosphere, directly impacting plasma and magnetic flux transport and auroral ac-
 367 tivity (Southwood & Kivelson, 2001; Cowley et al., 2003; Vogt et al., 2019; Nichols et
 368 al., 2019; Kita et al., 2019). While individual models typically quote some uncertainty
 369 in modeled arrival times (Tao et al., 2005; Zieger & Hansen, 2008; M. Owens et al., 2020),
 370 these uncertainties are often characterized relative to different standards and using dif-
 371 ferent methods, making cross-model comparisons difficult.

372 To allow direct comparisons of outer heliosphere solar wind models, independent
 373 quantification of modeled arrival time uncertainty can be performed with MMESH, as
 374 is common for near-Earth solar wind modeling (Gressl et al., 2014; Riley et al., 2018).
 375 The goal in quantifying the arrival time uncertainty is twofold: understanding the er-
 376 ror intrinsic to each model is necessary to give context to its forecasts, and character-
 377 izing these errors can give clues as to which aspects of the solar wind system an individ-
 378 ual model may not be capturing sufficiently. For both of these reasons, here we explore
 379 two methods available in MMESH of quantifying the arrival time uncertainties in the
 380 previously discussed models. These comparisons and uncertainty characterization are
 381 performed identically for every combination of spacecraft and model previously discussed;
 382 to keep illustrations of these informative and uncluttered, the *Juno* in-situ solar wind
 383 flow speed u_{mag} measurements will again be used alone.

384 3.2.1 Constant Time Offsetting

385 A simple metric to characterize the performance of a propagation model is to cal-
 386 culate the prediction efficiency, or correlation coefficient, between the propagated time
 387 series and an in-situ measurement of the same quantity (Zieger & Hansen, 2008; Kee-
 388 bler et al., 2022, e.g.). This offers a straightforward method to determine systematic, spacecraft-
 389 epoch-wide propagation model errors in the arrival time of shocks and other solar wind
 390 structures. The time span covered by the model can be shifted off that of the measured
 391 data by an offset time Δt both forward (i.e. later) and backward (i.e. earlier) in time,
 392 then the correlation coefficient between this offset model propagated time series and the
 393 in-situ measurements can be calculated and compared to the original.

394 Performing this $2n+1$ times for temporal offsets spanning the values $[-n, -n +$
 395 $\Delta t, \dots, n - \Delta t, n]$ for a realistic maximum offset time of $n \approx 4$ days (Tao et al., 2005;
 396 Zieger & Hansen, 2008) yields the correlation coefficient as a function of constant tem-
 397 poral offsets, $r(\Delta t)$, with positive temporal offsets indicating that the un-offset model
 398 leads the data and negative offsets indicating that the un-offset model lags the data. Max-
 399 imizing the correlation coefficient $r(\Delta t)$ thus gives a constant temporal offset which best
 400 aligns the propagation model with the measured time series; equivalently, this offset rep-
 401 resents a systematic error in the arrival time of the original model. There are two draw-
 402 backs to this method of accounting for temporal offsets in the model: first, it can only
 403 account for a constant temporal offset Δt , rather than a distribution of uncertainties or
 404 a time-varying offset; second, this metric conflates the temporal alignment of the time
 405 series with the magnitudes of their predicted values, and thus does not necessarily char-

acterize the model lag/lead time alone. Nonetheless, constant temporal offsetting is frequently used as a method to simply and quickly estimate model uncertainties, and as such remains available in MMESH.

3.2.2 Dynamic Time Warping

The performance of a solar wind propagation model can be decomposed into two components: the performance in modeling the arrival time and the performance in modeling the magnitude of the solar wind time series. These two are essentially represented by the abcissa and ordinate pairs of a propagated time series, respectively. Theoretically, differences between the propagation model and data time series should be decomposable by first optimizing the alignment of the model relative to the data to characterize the performance in arrival time, then secondly measuring the residuals between the aligned model and data time series to characterize the performance in magnitude. Aligning the model to the data in this way is often done by manually identifying patterns of shocks in both time series and calculating the difference in their observation times (e.g. Tao et al., 2005).

In practice, characterizing model performance in arrival time alone is not so straightforward, as the identification of patterns of shocks and shock-like structures in the solar wind data is often subjective. To more objectively define such structures, here we have “binarized” both the in-situ and propagation model time series data to identify extrema in both. The binarization process developed here involves taking the standard score (z-score) of the time derivative of a boxcar-smoothed time series and thresholding the result at a given significance level. This process has the end effect of identifying and isolating steep gradients in the time series of a given parameter, as would be expected in a shock, and is described in more detail in Appendix A and illustrated in A1. The binarization process was applied to the solar wind flow speed u_{mag} time series in both the model-propagated and in-situ data sets. The boxcar-smoothing-widths used for each time series and in each epoch were found dynamically and are listed in Table A1. Here a constant significance level of 3σ , measured across the full duration of each time series, has then been used for binarization.

Identifying shocks and shock-like structures in the now-binarized time series is trivial; aligning the patterns of structures found in the model and data time series is not, and remains subjective if performed manually. For reproducibility, here we employ an objective, automated method of aligning the two binarized time series based on the class of algorithms collectively known as dynamic time warping (DTW). Qualitatively, the aim of DTW is to locally shift, stretch, and compress one time series to better resemble another. DTW has only recently been applied to space weather modeling problems; the calculated net distance has been suggested as a useful, multi-scale metric for measuring the performance of solar wind models by Samara et al. (2022), and the resulting alignments have been used to create more accurate boundary conditions for solar wind propagation models by M. J. Owens and Nichols (2021). Within MMESH, the `dtw-python` package for the Python programming language developed by Giorgino (2009) is employed to warp the modeled time series to more closely resemble the in-situ data. The recommended usage, and that which will be followed in this discussion, is to use DTW to align the binarized model solar wind flow speed to the binarized measured flow speed, as the flow speed generally shows the clearest signatures of shocks and shock-like structures after binarization. Both the binarization and DTW methods within MMESH can, however, be applied independently to any of the propagated solar wind quantities (i.e. n , u_{mag} , p_{dyn} , or B_{IMF}) at the discretion of the user.

An overview of the two-series implementation of DTW is illustrated in Figure 4 and described here. This approach involves calculating the Euclidean distance between every permutation of the elements of each series, resulting in a two-dimensional matrix;

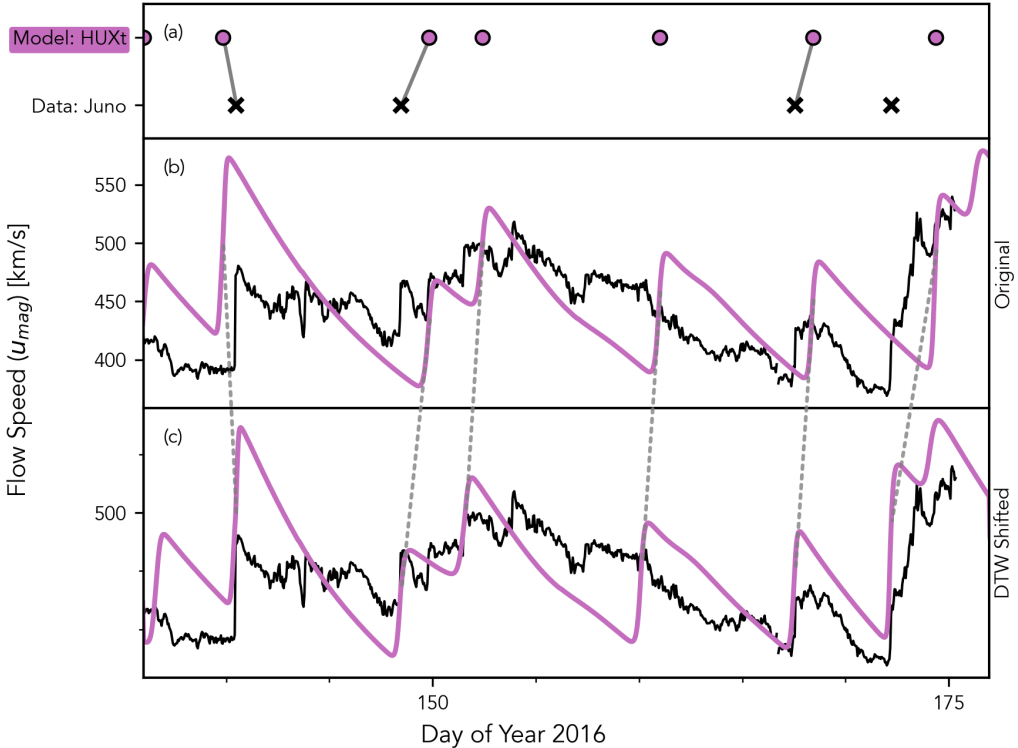


Figure 4. A composite diagram offering an overview of the dynamic time warping (DTW) process used to characterize model arrival time uncertainties. The (a) binarized model and data are shown as points representing the calculated extrema, with lines connecting model and data features which were identified to map to one another in the DTW process. The (b) original model and data time series are plotted to show the original alignment and may be compared to the (c) alignment of the warped model to the unchanged data, which demonstrates significantly reduced arrival time uncertainties. Dashed lines (b-c) connect the extrema identified in the original model to the same in the warped model; the horizontal component of these lines represents the offsets δt used to warp the model to best match the data. These δt are then taken as the distribution of arrival time uncertainties for the model.

a path, or alignment curve, through this matrix is then computed which minimizes the net distance, and this serves to effectively align the input modeled time series to best match the data by reindexing the former. DTW is here applied to the binarized time series data (Figure 4a) in order to eliminate the effect that each series' amplitude may have on the alignment calculation. From the aligned time series, tie points connecting the model time series to the data are then chosen from the alignment curve for each matching pair of model-data extrema (Figure 4a). The original model time series (Figure 4b) is then warped according to a linear interpolation of these tie points, which represents both the offsets of the matched extrema and the linear interpolations at each abscissa between these. The result is a warped time series which is better aligned with the spacecraft data (Figure 4c). While this process uses the binarized solar wind flow speed to compute the alignment, every parameter within a given model can then have the same warping applied to it. This allows for better alignment between all parameters, not just u_{mag} , by implicitly assuming that the input model parameters are aligned correctly with one another, and misaligned only relative to the measured data.

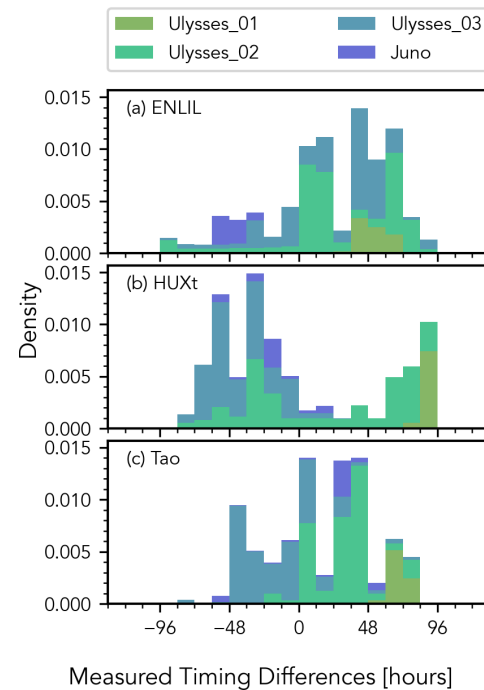
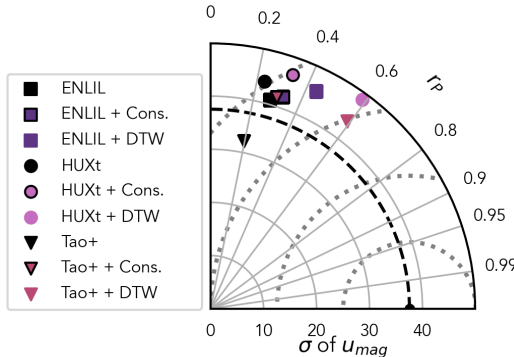


Figure 5. Histograms showing the distribution of total temporal shifts needed to best align each model with the in-situ data for the all spacecraft epochs, as found using dynamic time warping (DTW) as described in the text. The means of these distributions are equivalent to intrinsic shock arrival time errors, or timing biases, and the widths are representative of timing uncertainties.

472 For this demonstration of MMESH, DTW was used to align the binarized solar wind
 473 plasma flow speeds from each model to that of the data in each spacecraft epoch. Lim-
 474 its were placed on the DTW algorithm to ensure the resulting warped time series was
 475 physically meaningful: the maximum offsets allowed were ± 4 days (± 96 hours), chosen
 476 to be representative of the maximum temporal offsets measured in other studies (Tao
 477 et al., 2005; Zieger & Hansen, 2008). The first value of the modeled time series is forced
 478 to align to the first value of the measured time series by the DTW algorithm used here,
 479 as is the final value of the modeled time series to that of the measured. To account for
 480 this, the DTW process was applied to the same $2n + 1$ models with constant tempo-
 481 ral offsets in the range $[-n, n]$ and with step size Δt as was previously discussed in Sec-
 482 tion 3.2.1. The optimal alignment within these $2n+1$ DTW results was found by max-
 483 imizing the correlation coefficient of the warped model plasma flow speed u_{mag} to the
 484 data divided by the quasi- 1σ half-width of the distribution of total temporal offsets r/σ_P
 485 (i.e., both constant and dynamic temporal offsets combined). The total distributions of
 486 temporal offsets in each model are illustrated in Figure 5 for reference. These distribu-
 487 tions are not normally distributed, suggesting that the uncertainties in the modeled so-
 488 lar wind arrival times are not random, and are not centered at zero, indicating biases
 489 in the modeled arrival times.



490 **Figure 6.** A Taylor Diagram showing the performance of each model, before and after tempo-
 491 ral shifting, relative to the in-situ *Juno* solar wind data. The unshifted models (black symbols)
 492 all have correlation coefficient r in the range $0.2\sim 0.3$. Both constant time offsetting (outlined
 493 symbols) and DTW (full color symbols) improve the correlation coefficients of all models, but
 494 DTW improves the correlation coefficient more (r between $0.3\sim 0.4$ compared to r between
 495 $0.4\sim 0.6$, respectively). Employing time-varying temporal shifts is beneficial to matching the mod-
 496 els to the data more closely.

490 3.3 Prediction of Time-Varying Model Timing Uncertainties

491 The cross-model consistent characterization of systematic timing biases and un-
 492 certainties already discussed allows the performance of the solar wind models to be quan-
 493 titatively compared to one another. As the methods discussed in Section 3.2 rely on di-
 494 rect comparison to contemporaneous data, however, the timing biases and uncertainties
 495 cannot be empirically quantified in the absence of in-situ data— the main use case for so-
 496 lar wind modeling. To circumvent this, the distribution of timing uncertainties, as illus-
 497 trated in Figure 5, could be considered invariant in time and propagated as such; this
 498 method of propagating timing uncertainties is supported by MMESH. As these timing
 499 uncertainties and biases are known to vary in time, as can be seen by the different space-

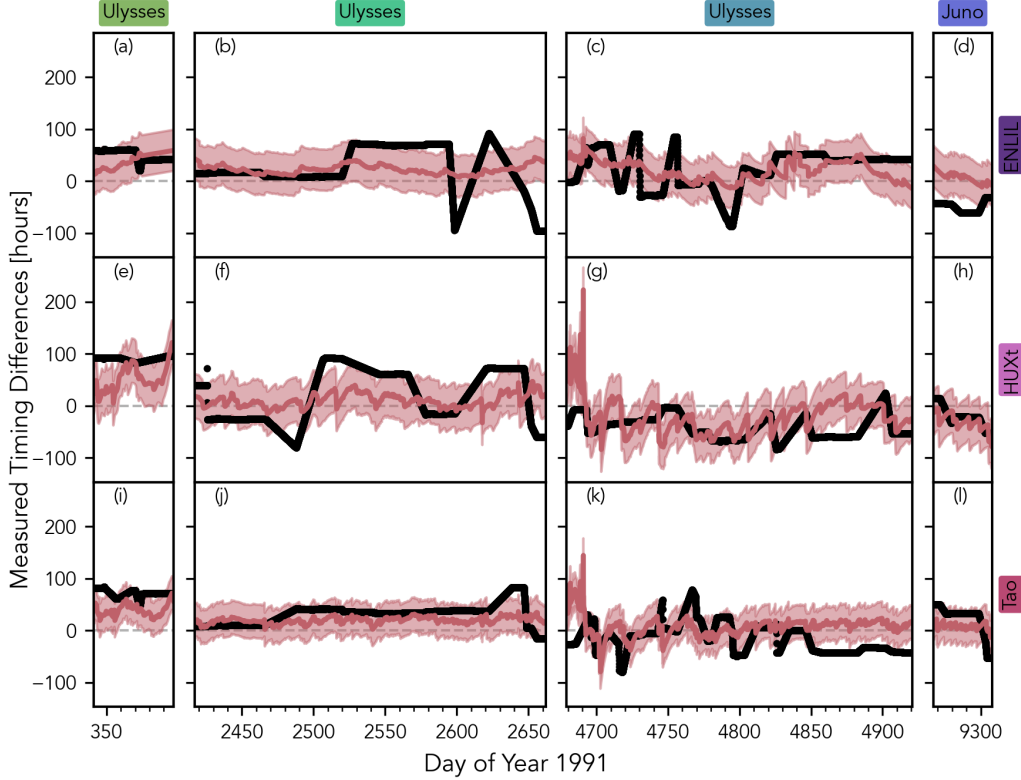


Figure 7. Plots of the measured temporal offsets (black lines) from DTW for each model-spacecraft-epoch set (e.g., a-d for ENLIL, e-h for HUXt, and i-l for Tao+), along with the multiple linear regression (MLR) fit to the temporal offsets found by fitting the offset time series with the parameters described in the text (red lines). While the independent parameters add significant variation in time, they nonetheless describe the empirical timing uncertainties and systematics fairly well. The 1σ prediction uncertainties in the MLR fit (shaded red regions) are also plotted.

500 craft epochs covered in Figure 5, this method has the drawback of explicitly overestimating
 501 the uncertainties at any given time.

502 Alternatively, MMESH also supports a simple- or multiple-linear regression model
 503 description of the timing uncertainties. Multiple linear regression models are simple mod-
 504 els which describe one continuous target variable as a linear combination of multiple con-
 505 tinuous predictor variables; simple linear regression refers to the special case of a single
 506 predictor variable. The coefficients calculated for each predictor variable thus describe
 507 the contributions of each to the target variable. Similarly, the estimated standard de-
 508 viation on these coefficients gives a sense of the relative importance of each predictor:
 509 relative to the coefficient value, a large standard deviation denotes a less significant pre-
 510 dictor, with the opposite being true for a relatively small standard deviation. The lin-
 511 ear regression method thus allows the propagation model timing uncertainties to be es-
 512 timated even in the absence of in-situ data for comparison, provided the values of each
 513 predictor variable are known.

514 As the input propagation models do not propagate measurement error, the arrival
 515 time uncertainties characterized previously are present due to the limitations of these
 516 MHD-based models, each of which makes different simplifications of the physics describ-

517 ing the solar wind. These simplification give rise to correlations between the timing un-
 518 certainties in these models and other physical parameters describing the solar wind en-
 519 vironment. Timing uncertainties in models with an inner boundary set by near-Earth
 520 measurements often trend with target-Sun-observer (TSO) angle in heliolongitude, in
 521 at least magnitude if not also in sign (Tao et al., 2005; Zieger & Hansen, 2008). Phys-
 522 ically, this trend represents increasing uncertainty in the solar wind conditions as sep-
 523 aration in heliolongitude (or Carrington longitude) increases away from the measurement
 524 point. While less commonly used, the offsets are expected to trend with the TSO an-
 525 gle in heliolatitude in a similar way, as the solar wind flow speed is known to be strongly
 526 ordered in heliolatitude during solar minimum (D. J. McComas et al., 2003; D. McCo-
 527 mas et al., 2008). This well-ordered structuring with heliolatitude breaks down during
 528 solar maximum (D. J. McComas et al., 2003), which further suggests a physical connec-
 529 tion between the offsets and the 11-year solar cycle. A final reasonable expectation is
 530 that the timing systematics and uncertainties are related to the models solar wind flow
 531 speed u_{mag} . This comes from the assumption that the propagation model is more likely
 532 to lag the data when underestimating the solar wind flow speed and more likely to lead
 533 when overestimating; if the underestimates tend to have lower magnitudes and overes-
 534 timates tend have larger magnitudes, then a trend between modeled solar wind flow speed
 535 and temporal offset is expected.

536 These physical relationships between total, time-variable model offsets and descrip-
 537 tive parameters about the state of the solar wind can be leveraged to estimate the model
 538 offsets in the absence of simultaneous in-situ data. Here, multiple linear regression has
 539 been employed to use all of these physical parameters (i.e. TSO angle in heliolongitude
 540 and heliolatitude, solar cycle phase, and modeled u_{mag}) as predictors of the time-variable
 541 timing uncertainties and biases by fitting the predictors to the combined spacecraft epochs
 542 during which simultaneous in-situ measurements are available, as illustrated in Figure
 543 7. Despite its simplicity, the multiple linear regression technique matches the known tem-
 544 poral offsets well. The combination of parameters used here accounts for 12% of the vari-
 545 ation in the measured timings for the ENLIL model (i.e., $R^2 = 0.12$), 37% in the HUXt
 546 model, and 20% in the Tao+ model.

547 3.4 Multi-Model Ensemble

548 An MME is now created by the combination of the propagation models. MMESH
 549 supports the creation of MMEs from input propagation models alone, from propagation
 550 models with characterized timing uncertainties, whether through constant time offset-
 551 ting or dynamic time warping, and from propagation models de-trended (i.e. warped)
 552 to account for timing biases with propagated uncertainties. Here, this final type of MME
 553 is created from the ENLIL, HUXt, and Tao+ solar wind propagation models warped ac-
 554 cording to the timing biases estimated by multiple linear regression to the multi-epoch
 555 in-situ dataset, and timing uncertainties propagated through.

556 For simplicity, an equal weights average of the each input model is taken. While
 557 there is some evidence that carefully-chosen weighting schemes may improve model per-
 558 formance (Guerra et al., 2020), more complicated weighting schemes may also decrease
 559 model performance compared to the equal weights, making equal weighting the more ro-
 560 bust choice (Genre et al., 2013). Thus, the only improvement on the simple equal-weights
 561 averaging scheme we impose is to set the weight to 0 when a model does not yield an
 562 output at a given time step, whether due to the model's design (e.g. the lack of param-
 563 eters other than solar wind flow speed in HUXt) or a lack of access to more recent mod-
 564 els. The resulting MME of solar wind flow speed is shown in Figure 8a, superimposed
 565 on the in-situ measurements of the *Juno* spacecraft during the missions's cruise phase
 (cf. Figure 3).

567 **3.4.1 Model Performance**

568 The performance of this multi-model, multi-epoch ensemble is summarized in Figure
 569 8, which shows that the ensemble has improved prediction efficiency of the solar wind
 570 flow speed u_{mag} during the *Juno* cruise epoch compared to any individual input model.
 571 All of the model time series, including that of the ensemble, show decreased standard
 572 deviations in Figure 8. This results from considering the distribution of timing uncer-
 573 tainties in calculating the mean values for each time series: when the distribution of tim-
 574 ing uncertainties is measured or predicted to be large, the shifted fore-shocks in the so-
 575 lar wind appear more ‘smoothed out’.

576 Despite this decreased standard deviation, the predicted flow speed u_{mag} of the MME
 577 ($r = 0.49$) outperforms ENLIL by 110% ($r = 0.23$), HUXt by 7% ($r = 0.46$), and
 578 Tao+ by 51% ($r = 0.32$) in correlation coefficient and achieves a centered root-mean-
 579 square difference (RMSD= 32.8) 28% lower than ENLIL (RMSD= 45.9), 14% lower
 580 than HUXt (RMSD= 38.1), and 9.1% lower than Tao+ (RMSD= 36.1). As HUXt does
 581 not contribute to parameters in the MME other than u_{mag} , and the performance of ENLIL
 582 beyond u_{mag} is poor here (i.e., ENLIL is evidently anticorrelated with the data in Fig-
 583 ure 8f-h), the MME underperforms Tao+ in n_{tot} , p_{dyn} , and B_{IMF} by 12%–24% in cor-
 584 relation coefficient with 5% – 8% larger RMSD. These shortcomings of the MME are
 585 thus slight, and would likely be reduced further or eliminated in epochs where ENLIL
 586 performs more similarly to Tao+; alternatively, adding new solar wind propagation mod-
 587 els to the MME discussed here would be expected to have a similar effect.

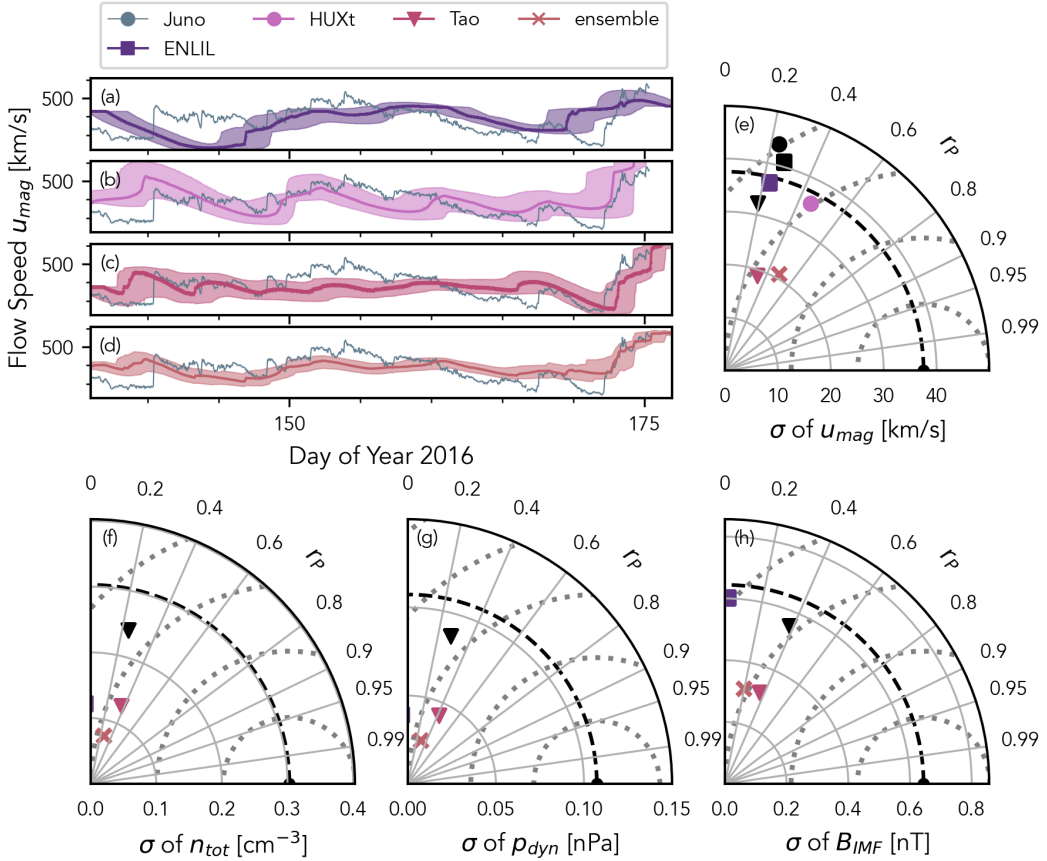


Figure 8. The solar wind flow speed u_{mag} , with timing uncertainties characterized by DTW and MLR applied over all spacecraft epochs, for (a) ENLIL, (b) HUXt, (c) Tao, and (d) the MME, compared to in-situ *Juno* data in each. The performance of the MME is summarized in the (e) Taylor diagram for u_{mag} , which illustrates that the MME outperforms all input models for this parameter; the Taylor diagram includes both the multi-epoch MLR-adjusted input models (colored symbols) and the original input models (black symbols) for comparison. Additional Taylor diagrams for (f) the total solar wind density n_{tot} , (g) the solar wind dynamic pressure p_{dyn} , and (h) the IMF magnitude B_{IMF} are included to show the performance of the MME in these parameters. As HUXt does not contribute to these parameters, the MME slightly underperforms Tao+.

588 **4 Juno-epoch Solar Wind MME for Jupiter**

589 Now that the multi-model epoch system has been fully described, all that remains
590 is to generate MMESH-propagated solar wind for a useful epoch. Here we have chosen
591 to run the ensemble for Jupiter contemporaneously with the *Juno* mission, beginning
592 before the spacecraft entered the planet's magnetosphere (2016/05/15) and continuing
593 seven years through mid-2023 (2023/05/15), in order to provide valuable context for the
594 upstream conditions near Jupiter during *Juno*'s mission. A subset of the ensemble model
595 results are shown in Figure 9, along with the results of the component models, spanning
596 the first 6 months of coverage provided by this MME. The *Juno* in-situ measurements
597 prior to entering Jupiter's magnetosphere are shown in Figure 9 for context, but as the
598 MME here is for Jupiter's location, rather than that of *Juno*, the two timeseries are not
599 expected to align as well as in Figure 9. The results of this specific MME are available
600 at <https://zenodo.org/link-to-specific-results>; more generally, the results of this
601 Jupiter MME along with any future updates to improve its predictive power or extend
602 the temporally coverage will be available, and documented, at <https://zenodo.org/link-to-all-results>.
603

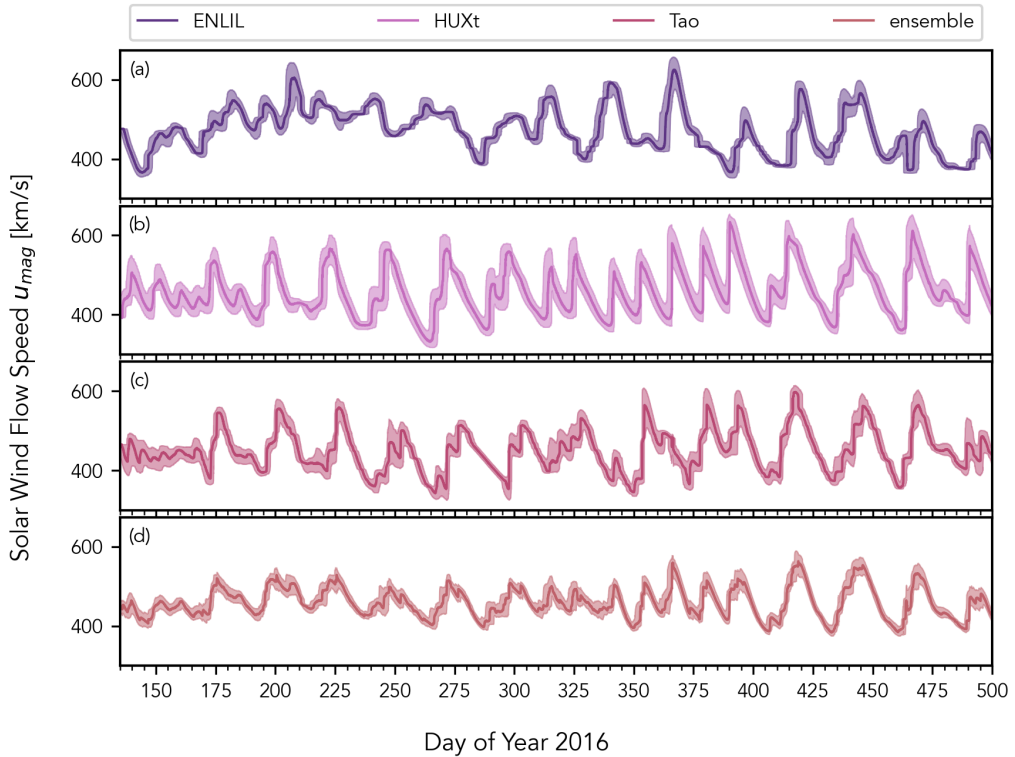


Figure 9. A 12-month subset of the *Juno*-era solar wind flow speed u_{mag} results, adjusted for timing biases measured using DTW and characterized using MLR, for the (a) ENLIL, (b) HUXt, (c) Tao+, and (d) MME, presented here starting during *Juno*'s approach to Jupiter in May 2016. The 1σ uncertainties in the solar wind flow speed u_{mag} are shown in each panel (shaded regions). Based on the results discussed here, the MME is expected to significantly outperform each of the component models in predicting the solar wind flow speed u_{mag} .

604

5 Summary and Conclusions

605 Here we have introduced MMESH, a Multi-Model Ensemble System for the He-
 606 liosphere, and described one use-case of this system to create a multi-model ensemble
 607 of the outer heliosphere solar wind near Jupiter through the first 7 years of *Juno* mis-
 608 sion, spanning 2016/07/04 – 2023/07/04.

609 MMESH provides a framework with two central objectives: first, to allow easy char-
 610 acterization of solar wind propagation model performance; and second, to create multi-
 611 model ensembles of the solar wind. The first objective is crucial to statistically eval-
 612 uating the strengths of the various solar wind propagation models available, as the orig-
 613 inal discussions of the performance of these models often quote different statistics or span
 614 non-overlapping epochs of the solar wind and thus cannot be compared one-to-one. Fur-
 615 ther, characterization of model performance yields an estimate of the model uncertainty,
 616 a quantity which is not provided internally by any model discussed here but which is es-
 617 sential for statistical analyses. With the second objective, we aim to create reliable com-
 618 posite models of the solar wind by combining physics-based solar wind propagation mod-
 619 els with their estimated variances to be used in statistical analyses of solar-wind-magnetosphere
 620 interactions throughout the solar system. The strength of ensemble modeling lies in lever-
 621 aging the different strengths of the constituent models, and so these two objectives are
 622 closely intertwined.

623 MMESH additionally includes a method to compare biases and variances in the model
 624 timing to physical parameters across disparate epochs prior to creating an ensemble. The
 625 objective of this multi-epoch method is to de-trend biases in the model timing which may
 626 arise from the various assumptions and simplifications made by each model. De-trending
 627 is performed here through multiple linear regression (MLR) of the measured model tim-
 628 ing biases with a subset of the physically reasonable parameters with which model per-
 629 formance is expected to vary. The phase of the solar cycle, difference in heliolongitude
 630 and heliolatitude between the model target and the observer, and the modeled solar wind
 631 flow speed are all reasonable and considered here. As estimation of the model timing bi-
 632 ases and variances is only possible when contemporaneous in-situ data are available for
 633 comparison, the spans over which the MLR de-trending can be performed are limited.
 634 The MLR de-trending is made more robust by considering multiple disparate epochs dur-
 635 ing which spacecraft data are available.

636 Using all of these methods, a multi-model ensemble of the solar wind conditions
 637 at Jupiter during the *Juno*-epoch has been created by combining three physics-based so-
 638 lar wind propagation models (ENLIL, HUXt, and Tao+); the version of this ensemble
 639 discussed here is available at <https://zenodo.org/link-to-specific-results> and
 640 the latest release of is available at <https://zenodo.org/link-to-all-results>. Biases
 641 and variances in each models timing were characterized for four epochs during which *Ulysses*
 642 or *Juno* data were available for comparison, spanning in total from 1991/12/08 – 2016/06/29.
 643 The model timing biases were then de-trended using MLR to the heliolatitude and mod-
 644 eled flow speed, which were determined to provide the best balance between describing
 645 the timing biases and overfitting. The biases in the three constituent solar wind mod-
 646 els were corrected according to the MLR equation for the full MME span of 2016/07/04
 647 – 2023/07/04 and combined. The resulting ensemble model outperforms all of the con-
 648 stituent models relative to the *Juno* cruise data immediately preceding this epoch; the
 649 ensemble has a correlation coefficient of 0.41 (78% increase over ENLIL, 32% increase
 650 over HUXt, and 86% increase over Tao+, after accounting for timing offsets in each). The
 651 improved upstream solar wind monitoring capabilities demonstrated by this MME are
 652 available to be downloaded and used immediately, and should prove crucial to ongoing
 653 and future in-situ studies of the Jovian magnetosphere using *Galileo*, *Juno*, JUICE, and
 654 *Europa Clipper*, as well as remote sensing studies using observatories such as JWST, HST,
 655 and Chandra.

656 **Appendix A Time Series Binarization**

657 Here, the measured and modeled magnitude of the solar wind flow speed u_{mag} is
 658 post-processed by first smoothing the series, then taking the standard score of its time
 659 derivative. Smoothing is accomplished by taking a rolling boxcar average of the flow speed
 660 u_{mag} . Smoothing in this way serves as a low-pass filter, allowing the recovery of the large-
 661 scale shape of the time series while ignoring small-scale fluctuations, which may dom-
 662 inate in in-situ spacecraft measurements. The time derivative of the flow speed time se-
 663 ries $u_{mag}(t)$ is chosen in order to better identify the transition of a spacecraft or model
 664 trajectory through a slow-fast wind interface; these increases in solar wind flow speed
 665 occur over timescales less than 1hour and are more easily identifiable than changes in
 666 other solar wind parameters, which typically occur over longer timescales. The standard-
 667 score of the time series, or the time series normalized to its own standard deviation, al-
 668 lows for direct comparison of the relative changes between different time series which may
 669 have widely varying mean values.

670 Binarization requires subjective input of a boxcar-smoothing-width and significance
 671 level for each time series, however these parameters are partially degenerate with one
 672 another– a smaller smoothing window and a higher significance level will yield similar
 673 results to a larger window with lower significance level. To limit subjectivity, boxcar-smoothing-
 674 widths are found for each time series within a given epoch as the smallest width which,
 675 when applied to each time series before the derivative is taken, results in an equal se-
 676 ries standard deviation to the smallest such standard deviation in the epoch. Qualita-
 677 tively, this is the boxcar-smoothing-width required to make each time series look as "smooth"
 678 as the "smoother" time series of the epoch. The boxcar-smoothing-widths used for each
 679 time series and in each epoch are listed in Table A1.

Table A1. Boxcar-smoothing widths for binarization, in hours

Source	Epoch			
	Ulysses 1	Ulysses 2	Ulysses 3	Juno
in-situ	5	15	2	7
ENLIL	8	1	4	5
HUXt	1	9	1	1
Tao+	6	11	2	10

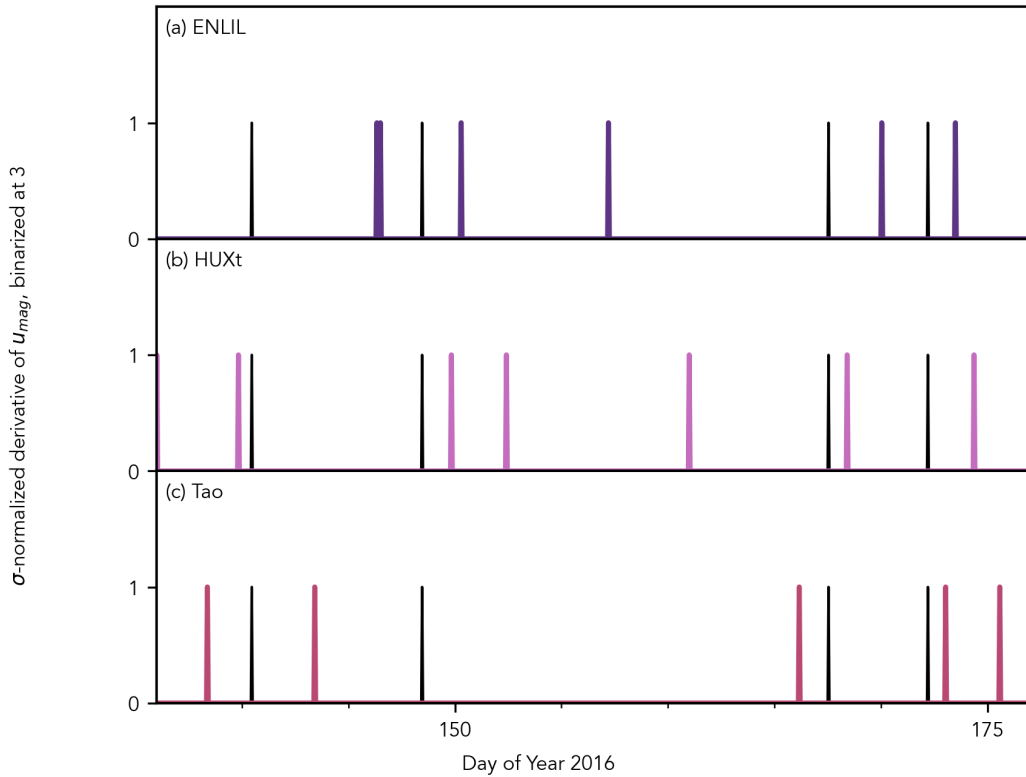


Figure A1. Binarized time series of the solar wind flow speed u_{mag} for the (a) ENLIL, (b) HUXt, and (c) Tao+ solar wind propagation models, with the binarized time series of the in-situ *Juno* data superimposed on each (black lines). The time-derivatives of all these series have been binarized at a value of 3σ , such that each ‘spike’ represents a change in the time-derivative of 3σ or larger.

680 **Open Research**

681 The results presented in this document rely on data collected by the Solar Radio
 682 Monitoring Program (<https://www.spaceweather.gc.ca/forecast-precision/solar>
 683 -solaire/solarflux/sx-en.php) with additional processing by the NOAA National
 684 Centers for Environmental Information (<https://www.ncei.noaa.gov/>). These data
 685 were accessed via the LASP Interactive Solar Irradiance Datacenter (LISIRD) (<https://lasp.colorado.edu/lisird/>). Ephemeris information was obtained by use of the NASA
 686 Navigation and Ancillary Information Facility (NAIF) SPICE toolkit.
 687

688 Simulation results for the ENLIL solar wind propagation model (version 2.8f) have
 689 been provided by the Community Coordinated Modeling Center (CCMC) at Goddard
 690 Space Flight Center through their publicly available simulation services (<https://ccmc.gsfc.nasa.gov>). The ENLIL Model was developed by Dusan Odstrcil at George Ma-
 691 son University. Spacecraft data were acquired from the Goddard Space Flight Center
 692 Space Physics Data Facility (SPDF) COHOBWeb service, except for the *Juno* in-situ data,
 693 which were instead acquired from Wilson et al. (2018) (plasma data) and the Automated
 694 Multi-Dataset Analysis web tool hosted at <https://amda.irap.omp.eu/>.
 695

696 The MMESH code is available at <https://github.com/mjrutala/MMESH>, and in-
 697 cludes the routines used to create the figures shown here. The *Juno*-epoch MME pre-
 698 sented here is available at <https://zenodo.org/link-to-specific-results>, and fu-
 699 ture updates to this MME will be accessible from <https://zenodo.org/link-to-all-results>.
 700

701 **Acknowledgments**

702 MJR's and CMJ's work at DIAS was supported by Science Foundation Ireland Grant
 703 18/FRL/6199.

704 **References**

705 Arge, C. N., & Pizzo, V. J. (2000). Improvement in the prediction of solar
 706 wind conditions using near-real time solar magnetic field updates. *Journal of Geophysical Research: Space Physics*, 105(A5), 10465–10479. doi:
 707 10.1029/1999JA000262

708 Balogh, A., Beek, T. J., Forsyth, R. J., Hedgecock, P. C., Marquedant, R. J., Smith,
 709 E. J., ... Tsurutani, B. T. (1992, January). The magnetic field investigation
 710 on the ULYSSES mission - Instrumentation and preliminary scientific results. ,
 711 92(2), 221–236.

712 Bame, S. J., McComas, D. J., Barraclough, B. L., Phillips, J. L., Sofaly, K. J.,
 713 Chavez, J. C., ... Sakurai, R. K. (1992, January). The ULYSSES solar
 714 wind plasma experiment. , 92(2), 237–265.

715 Barnard, L., & Owens, M. (2022, October). HUXt—An open source, computa-
 716 tionally efficient reduced-physics solar wind model, written in Python. *Frontiers in
 717 Physics*, 10, 1005621. doi: 10.3389/fphy.2022.1005621

718 Borovsky, J. E., & Denton, M. H. (2010). Solar wind turbulence and shear: A
 719 superposed-epoch analysis of corotating interaction regions at 1 AU. *Journal of
 720 Geophysical Research: Space Physics*, 115(A10). doi: 10.1029/2009JA014966

721 Connerney, J. E. P., Benn, M., Bjarno, J. B., Denver, T., Espley, J., Jorgensen,
 722 J. L., ... Smith, E. J. (2017, November). The juno magnetic field investiga-
 723 tion. , 213(1-4), 39–138. doi: 10.1007/s11214-017-0334-z

724 Cowley, S. W. H., Bunce, E. J., & Nichols, J. D. (2003). Origins of Jupiter's main
 725 oval auroral emissions. *Journal of Geophysical Research: Space Physics*,
 726 108(A4). doi: 10.1029/2002JA009329

727 Crooker, N. U., Gosling, J. T., Bothmer, V., Forsyth, R. J., Gazis, P. R., Hewish,
 728

729 A., ... Wimmer-Schweingruber, R. F. (1999, July). CIR morphology,
 730 turbulence, discontinuities, and energetic particles. , 89, 179–220. doi:
 731 10.1023/A:1005253526438

732 Ebert, R. W., Bagenal, F., McComas, D., & Fowler, C. (2014, September). A
 733 survey of solar wind conditions at 5 AU: A tool for interpreting solar wind-
 734 magnetosphere interactions at Jupiter. *Frontiers in Astronomy and Space
 735 Sciences*, 1, 4. doi: 10.3389/fspas.2014.00004

736 Ebert, R. W., McComas, D. J., Bagenal, F., & Elliott, H. A. (2010, December).
 737 Location, structure, and motion of Jupiter's dusk magnetospheric boundary
 738 from ~1625 to 2550 R_J. *Journal of Geophysical Research (Space Physics)*,
 739 115(A12223), A12223. doi: 10.1029/2010JA015938

740 Ebert, R. W., McComas, D. J., Elliott, H. A., Forsyth, R. J., & Gosling, J. T. (2009,
 741 January). Bulk properties of the slow and fast solar wind and interplanetary
 742 coronal mass ejections measured by Ulysses: Three polar orbits of observa-
 743 tions. *Journal of Geophysical Research (Space Physics)*, 114(A1), A01109. doi:
 744 10.1029/2008JA013631

745 Elvidge, S., Granados, S. R., Angling, M. J., Brown, M. K., Themens, D. R., &
 746 Wood, A. G. (2023). Multi-model ensembles for upper atmosphere models.
 747 *Space weather : the international journal of research & applications*, 21(3),
 748 e2022SW003356. doi: 10.1029/2022SW003356

749 Genre, V., Kenny, G., Meyler, A., & Timmermann, A. (2013). Combining expert
 750 forecasts: Can anything beat the simple average? *International Journal of
 751 Forecasting*, 29(1), 108–121. doi: 10.1016/j.ijforecast.2012.06.004

752 Giorgino, T. (2009). Computing and visualizing dynamic time warping alignments
 753 in R: The dtw package. *Journal of Statistical Software*, 31(7), 1–24. doi: 10
 754 .18637/jss.v031.i07

755 Gosling, J., & Pizzo, V. (1999, July). Formation and Evolution of Corotating Inter-
 756 action Regions and their Three Dimensional Structure. *Space Science Reviews*,
 757 89(1), 21–52. doi: 10.1023/A:1005291711900

758 Gressl, C., Veronig, A. M., Temmer, M., Odstrčil, D., Linker, J. A., Mikić, Z., & Ri-
 759 ley, P. (2014, May). Comparative study of MHD modeling of the background
 760 solar wind. , 289(5), 1783–1801. doi: 10.1007/s11207-013-0421-6

761 Guerra, J. A., Murray, S. A., Bloomfield, D. S., & Gallagher, P. T. (2020,
 762 July). Ensemble forecasting of major solar flares: Methods for combin-
 763 ing models. *Journal of Space Weather and Space Climate*, 10(38), 38. doi:
 764 10.1051/swsc/2020042

765 Hagedorn, R., Doblas-Reyes, F. J., & Palmer, T. N. (2005, January). The rationale
 766 behind the success of multi-model ensembles in seasonal forecasting — I. Basic
 767 concept. *Tellus Series A*, 57(3), 219–233. doi: 10.3402/tellusa.v57i3.14657

768 Hanlon, P. G., Dougherty, M. K., Forsyth, R. J., Owens, M. J., Hansen, K. C.,
 769 Tóth, G., ... Young, D. T. (2004, September). On the evolution of the solar
 770 wind between 1 and 5 AU at the time of the Cassini Jupiter flyby: Multi-
 771 spacecraft observations of interplanetary coronal mass ejections including the
 772 formation of a merged interaction region. *Journal of Geophysical Research
 773 (Space Physics)*, 109(A09S03), A09S03. doi: 10.1029/2003JA010112

774 Kasper, J. C. (2002). *Solar Wind Plasma: Kinetic Properties and Micro-Instabilities*
 775 (Unpublished doctoral dissertation). Massachusetts Institute of Technology,
 776 Cambridge, MA..

777 Keebler, T. B., Tóth, G., Zieger, B., & Opher, M. (2022, June). MSWIM2D: Two-
 778 dimensional outer heliosphere solar wind modeling. , 260(2), 43. doi: 10.3847/
 779 1538-4365/ac67eb

780 King, J. H., & Papitashvili, N. E. (2005, February). Solar wind spatial scales in and
 781 comparisons of hourly Wind and ACE plasma and magnetic field data. *Journal
 782 of Geophysical Research (Space Physics)*, 110(A02104), A02104. doi: 10.1029/
 783 2004JA010649

784 Kita, H., Kimura, T., Tao, C., Tsuchiya, F., Murakami, G., Yamazaki, A., ... Fujimoto, M. (2019, December). Jovian UV Aurora's Response to the Solar Wind:
 785 Hisaki EXCEED and Juno Observations. *Journal of Geophysical Research: Space Physics*, *124*(12), 10,209–10,218. doi: 10.1029/2019JA026997

786 Lepping, R. P., Acuña, M. H., Burlaga, L. F., Farrell, W. M., Slavin, J. A., Schatten, K. H., ... Worley, E. M. (1995, February). The wind magnetic field investigation. , *71*(1-4), 207–229. doi: 10.1007/BF00751330

787 McComas, D., Allegrini, F., Bagenal, F., Casey, P., Delamere, P., Demkee, D., ... Weidner, S. (2008, October). The solar wind around pluto (SWAP) instrument aboard new horizons. , *140*(1-4), 261–313. doi: 10.1007/s11214-007-9205-3

788 McComas, D. J., Alexander, N., Allegrini, F., Bagenal, F., Beebe, C., Clark, G., ... White, D. (2017, November). The Jovian Auroral Distributions Experiment (JADE) on the Juno Mission to Jupiter. *Space Science Reviews*, *213*(1-4), 547–643. doi: 10.1007/s11214-013-9990-9

789 McComas, D. J., Angold, N., Elliott, H. A., Livadiotis, G., Schwadron, N. A., Skoug, R. M., & Smith, C. W. (2013, December). Weakest solar wind of the space age and the current “Mini” solar maximum. , *779*(2), 2. doi: 10.1088/0004-637X/779/1/2

790 McComas, D. J., Bame, S. J., Barraclough, B. L., Feldman, W. C., Funsten, H. O., Gosling, J. T., ... Neugebauer, M. (1998, January). Ulysses' return to the slow solar wind. , *25*(1), 1–4. doi: 10.1029/97GL03444

791 McComas, D. J., Elliott, H. A., Schwadron, N. A., Gosling, J. T., Skoug, R. M., & Goldstein, B. E. (2003, May). The three-dimensional solar wind around solar maximum. , *30*(10), 1517. doi: 10.1029/2003GL017136

792 McComas, D. J., Gosling, J. T., & Skoug, R. M. (2000, August). Ulysses observations of the irregularly structured mid-latitude solar wind during the approach to solar maximum. , *27*(16), 2437–2440. doi: 10.1029/2000GL000052

793 Murray, S. A. (2018). The importance of ensemble techniques for operational space weather forecasting. *Space weather : the international journal of research & applications*, *16*(7), 777–783. doi: 10.1029/2018SW001861

794 Nichols, J. D., Kamran, A., & Milan, S. E. (2019). Machine learning analysis of jupiter's far-ultraviolet auroral morphology. *Journal of Geophysical Research: Space Physics*, *124*(11), 8884–8892. doi: 10.1029/2019JA027120

795 Odstrcil, D. (2003, August). Modeling 3-D solar wind structure. *Advances in Space Research*, *32*(4), 497–506. doi: 10.1016/S0273-1177(03)00332-6

796 Owens, M., Lang, M., Barnard, L., Riley, P., Ben-Nun, M., Scott, C. J., ... Gonzi, S. (2020, March). A computationally efficient, time-dependent model of the solar wind for use as a surrogate to three-dimensional numerical magnetohydrodynamic simulations. , *295*(3), 43. doi: 10.1007/s11207-020-01605-3

797 Owens, M. J. (2018, August). Solar Wind and Heavy Ion Properties of Interplanetary Coronal Mass Ejections. *Solar Physics*, *293*(8), 122. doi: 10.1007/s11207-018-1343-0

798 Owens, M. J., & Nichols, J. D. (2021, December). Using in situ solar-wind observations to generate inner-boundary conditions to outer-heliosphere simulations - I. Dynamic time warping applied to synthetic observations. , *508*(2), 2575–2582. doi: 10.1093/mnras/stab2512

799 Palmerio, E., Nieves-Chinchilla, T., Kilpua, E. K. J., Barnes, D., Zhukov, A. N., Jian, L. K., ... Sánchez-Cano, B. (2021). Magnetic structure and propagation of two interacting CMEs from the sun to saturn. *Journal of Geophysical Research: Space Physics*, *126*(11), e2021JA029770. doi: 10.1029/2021JA029770

800 Papitashvili, N. E., & King, J. H. (2020). *OMNI Hourly Data*. NASA Space Physics Data Facility. doi: 10.48322/1shr-ht18

801 Richardson, I. G. (2018, January). Solar wind stream interaction regions throughout the heliosphere. *Living Reviews in Solar Physics*, *15*(1), 1. doi: 10.1007/s41116-017-0011-z

Richardson, J. D., Paularena, K. I., Lazarus, A. J., & Belcher, J. W. (1995, February). Radial evolution of the solar wind from IMP 8 to Voyager 2. , *22*(4), 325–328. doi: 10.1029/94GL03273

Riley, P., Mays, M. L., Andries, J., Amerstorfer, T., Biesecker, D., Delouille, V., ... Zhao, X. (2018). Forecasting the arrival time of coronal mass ejections: Analysis of the CCMC CME scoreboard. *Space weather : the international journal of research & applications*, *16*(9), 1245–1260. doi: 10.1029/2018SW001962

Samara, E., Laperre, B., Kieokaew, R., Temmer, M., Verbeke, C., Rodriguez, L., ... Poedts, S. (2022, March). Dynamic time warping as a means of assessing solar wind time series. , *927*(187), 187. doi: 10.3847/1538-4357/ac4af6

Sanchez-Diaz, E., Rouillard, A. P., Lavraud, B., Segura, K., Tao, C., Pinto, R., ... Plotnikov, I. (2016). The very slow solar wind: Properties, origin and variability. *Journal of Geophysical Research: Space Physics*, *121*(4), 2830–2841. doi: 10.1002/2016JA022433

Slavin, J. A., Smith, E. J., Spreiter, J. R., & Stahara, S. S. (1985, July). Solar wind flow about the outer planets: Gas dynamic modeling of the jupiter and saturn bow shocks. , *90*(A7), 6275–6286. doi: 10.1029/JA090iA07p06275

Smith, C. W., L'Heureux, J., Ness, N. F., Acuña, M. H., Burlaga, L. F., & Scheifele, J. (1998, July). The ACE magnetic fields experiment. , *86*, 613–632. doi: 10.1023/A:1005092216668

Southwood, D. J., & Kivelson, M. G. (2001). A new perspective concerning the influence of the solar wind on the Jovian magnetosphere. *Journal of Geophysical Research: Space Physics*, *106*(A4), 6123–6130. doi: 10.1029/2000JA000236

Tao, C., Kataoka, R., Fukunishi, H., Takahashi, Y., & Yokoyama, T. (2005, November). Magnetic field variations in the Jovian magnetotail induced by solar wind dynamic pressure enhancements. *Journal of Geophysical Research (Space Physics)*, *110*(A11), A11208. doi: 10.1029/2004JA010959

Taylor, K. E. (2001, April). Summarizing multiple aspects of model performance in a single diagram. , *106*(D7), 7183–7192. doi: 10.1029/2000JD900719

Tsurutani, B. T., Gonzalez, W. D., Gonzalez, A. L. C., Guarneri, F. L., Gopalswamy, N., Grande, M., ... Vasyliunas, V. (2006). Corotating solar wind streams and recurrent geomagnetic activity: A review. *Journal of Geophysical Research: Space Physics*, *111*(A7). doi: 10.1029/2005JA011273

Vogt, M. F., Gyalay, S., Kronberg, E. A., Bunce, E. J., Kurth, W. S., Zieger, B., & Tao, C. (2019, December). Solar wind interaction with jupiter's magnetosphere: A statistical study of galileo in situ data and modeled upstream solar wind conditions. *Journal of Geophysical Research (Space Physics)*, *124*(12), 10,170–10,199. doi: 10.1029/2019JA026950

Wilson, R. J., Bagenal, F., Valek, P. W., McComas, D. J., Allegrini, F., Ebert, R. W., ... Thomsen, M. F. (2018, April). Solar Wind Properties During Juno's Approach to Jupiter: Data Analysis and Resulting Plasma Properties Utilizing a 1-D Forward Model. *Journal of Geophysical Research: Space Physics*, *123*(4), 2772–2786. doi: 10.1002/2017JA024860

Xie, H., Ofman, L., & Lawrence, G. (2004, March). Cone model for halo CMEs: Application to space weather forecasting. *Journal of Geophysical Research (Space Physics)*, *109*(A03109), A03109. doi: 10.1029/2003JA010226

Zhao, X. P., Plunkett, S. P., & Liu, W. (2002). Determination of geometrical and kinematical properties of halo coronal mass ejections using the cone model. *Journal of Geophysical Research: Space Physics*, *107*(A8), SSH 13-1-SSH 13-9. doi: 10.1029/2001JA009143

Zieger, B., & Hansen, K. C. (2008, August). Statistical validation of a solar wind propagation model from 1 to 10 AU. *Journal of Geophysical Research (Space Physics)*, *113*(A8), A08107. doi: 10.1029/2008JA013046

Zurbuchen, T. H., & Richardson, I. G. (2006, March). In-Situ Solar Wind and Magnetic Field Signatures of Interplanetary Coronal Mass Ejections. *Space Science*

